Theoretical study of the unusual potential energy curve of the $A\,^1\Sigma^+$ state of AgH

Henryk A. Witek,[a] Dmitri G. Fedorov, and Kimihiko Hirao
Department of Applied Chemistry, Graduate School of Engineering, The University of Tokyo, Tokyo, 113-8656 Japan

Alexandra Viel
Department of Chemistry and Kenneth S. Pitzer Center for Theoretical Chemistry, University of California, Berkeley, California 94720-1460

Per-Olof Widmark
Department of Theoretical Chemistry, University of Lund, Chemical Center, P.O.B 124, S-221 00 Lund, Sweden

(Received 20 December 2001; accepted 6 February 2002)

The $A\,^1\Sigma^+$ potential energy curve of AgH is studied by means of the second-order multistate multireference perturbation theory including the spin–orbit and relativistic effects. The anomalous behavior of the vibrational energy levels observed in experiment is reproduced well by theory. An analysis of the $A\,^1\Sigma^+$ wave function shows that at the internuclear distance of 4–6 Å, a partial electron transfer from the $5p_z$ orbital of silver to the $1s$ orbital of hydrogen occurs. This admixture of the ionic-like [core] $4d^{10}1s_H^2$ configuration occurring in $A\,^1\Sigma^+$ due to two avoided crossings, namely $X\,^1\Sigma^+$ with $A\,^1\Sigma^+$ and $A\,^1\Sigma^+$ with $C\,^1\Sigma^+$, is found to be responsible for the unusual shape of the $A\,^1\Sigma^+$ potential energy curve: the effective potential is a superposition of a Morse-like covalent interaction between Ag and H, and the electrostatic ionic-like interaction between Ag^+ and H^-. We present spectroscopic parameters, vibrational levels, and rotational constants computed for a large number of vibrational levels and observe good agreement with available experimental data. The equilibrium distance agrees within 0.01 Å and the vibrational frequency within 60 cm^{-1} for the state-specific calculations. Larger relative discrepancy is observed for $\omega_e x_e$, about 30 cm^{-1}, however the non-Morse-like nature of the energy curve makes it impossible to describe the levels only with ω and $\omega_e x_e$, so that direct comparison is not well defined. © *2002 American Institute of Physics.* [DOI: 10.1063/1.1465403]

I. INTRODUCTION

The peculiar shape of the $A\,^1\Sigma^+$ potential energy curve of AgH attracted some attention over the last 70 years. First experimental work on $A\,^1\Sigma^+$ was done by Bengtsson and Olsson[1] in 1931. They analyzed the $A\,^1\Sigma^+ \rightarrow X\,^1\Sigma^+$ emission spectra and determined vibrational levels and spectroscopic parameters for both investigated states. One of their findings was an anomalous behavior of vibrational levels for $A\,^1\Sigma^+$, well illustrated in the Birge–Sponer diagram. In this plot, showing a relationship between the vibrational interval $\Delta G(v+\frac{1}{2})$ and the vibrational quantum number v, the vibrational levels with $v=4$, $v=5$, and $v=6$ deviate strongly from the usual linear shape characteristic for Morse-like potentials. Similar behavior is also found for rotational constants. Gerö and Schmid[2] suggested in 1943 that this anomaly results from perturbations caused by the $B\,^1\Sigma^+$ state. However, as noted by Learner,[3] such perturbation is usually on the order of a few cm^{-1}, while for $A\,^1\Sigma^+$ the levels are displaced by several thousand wave numbers. Moreover, the experimental investigation of $B\,^1\Sigma^+$ done by Ringström and Åslund[4] in 1965 shows no evident signs of such a perturbation. A different approach is presented by Learner;[3] he explains the irregularities of the spectrum in terms of an anomalous potential for the $A\,^1\Sigma^+$ state. His potential is constructed by means of several techniques. Around equilibrium, a Morse curve is used employing the constants derived for the Dunham function for $v=1,2,3$; this Morse curve is also used to determine the $A\,^1\Sigma^+$ potential at short distances. For larger distances, the potential is derived using Klein's method, which was used to determine the half width of the curve at all v from 4 to 7 by graphical methods, and for $v=10$ and $v=16$ by means of unobserved levels inferred from the modified Birge–Sponer diagram. The constructed curve is very different from the usual potential observed for diatomic systems. Its shape is explained by Learner in terms of an avoided crossing of two $^1\Sigma^+$ states arising from the atomic ^2P and ^2D states of silver. However, Ringström and Åslund[4] did not support this hypothesis in their experimental investigation of the low-lying states of AgH: $B\,^1\Sigma^+$, arising from the ^2D state of Ag, was found to have a similar characteristic to other states arising from ^2D.

Theoretical investigation of potential energy curves of AgH is challenging: it requires simultaneous account for relativistic, correlation, and spin–orbit effects. Hess and Chandra[5] performed spin-free relativistic CI calculations on the $A\,^1\Sigma^+$ potential energy curve of AgH only near the equilibrium geometry. In this region, the obtained potential does

[a]Author to whom correspondence should be addressed; electronic mail: cedziu@qcl.t.u-tokyo.ac.jp

not show any peculiarities. Extensive study of the potential energy curves arising from the atomic ^2S, ^2P, and ^2D states of silver is performed by Witek *et al.*[6] by means of relativistic multireference perturbation theory combined with the spin-orbit complete active space (CAS) configuration interaction (CI) method. The calculated $A\,^1\Sigma^+$ curve exhibits similar qualitative features to the curve obtained by Learner, however, the flat plateau in Learner's curve is replaced by a mild slope in the theoretical potential.

No vibrational energy levels were calculated for neither proposed potentials. Therefore, the definitive discussion of the shape of the $A\,^1\Sigma^+$ potential energy curve of AgH would require solving the nuclear motion problem and comparing obtained vibrational levels with experiment. The present work brings such a comparison. The use of a larger active space and multistate formalism allows the authors to determine an accurate $A\,^1\Sigma^+$ potential energy curve. A numerical scheme is used to solve the nuclear motion problem for all potential energy curves, the one derived graphically by Learner and the ones computed by us. The obtained vibrational levels and rotational constants are compared to experimental data. A detailed analysis of the $A\,^1\Sigma^+$ electronic wave function is also performed in order to explain the unusual shape of the potential.

II. COMPUTATIONAL METHODS

A. Computation of the potential energy curves

The primitive basis set for Ag is constructed by optimizing a $23s14p11d$ set with respect to the average energy for the two states: $^2S(d^{10}s)$ and $^2D(d^9s^2)$. This is done at the self-consistent field (SCF) level with the second order Douglas–Kroll Hamiltonian.[7] The generator formula

$$\ln(\zeta_k)=c_{-1}/k+c_0+c_1k,\quad k=1,2,... \tag{2.1}$$

is used and the three parameters c_{-1}, c_0, and c_1 are optimized. The $23s14p11d$ set is augmented to a $24s17p12d$ set to yield a good and balanced description of the three states $^2S(d^{10}s)$, $^2D(d^9s^2)$, and $^2P(d^{10}p)$ at the averaged coupled pair functional[8] (ACPF) level. The extension is done by continuing the generator formula above. A polarizing set consisting of $4f3g$ functions is optimized as an even-tempered set with respect to the average energy of $^2S(d^{10}s)$, $^2D(d^9s^2)$ and $^2P(d^{10}p)$ at the ACPF level. The primitives with largest exponent are contracted at the restricted Hartree–Fock level using the relativistic elimination of small component (RESC) Hamiltonian:[9] $(14s10p6d)$ contracted to $[3s3p2d]$, the remaining exponents are left uncontracted, $10s7p6d4f3g$. The resultant basis set is given in Tables I and II. The basis set used for H is cc-pVQZ.[10]

In order to treat relativistic effects, we employ the RESC method. Internal uncontraction of the atomic orbitals in constructing the RESC matrices is used throughout, to improve resolution of the identity used in RESC. The molecular orbital space is chosen in spherical harmonics. In order to optimize the orbitals, we use the CAS self-consistent field (CASSCF) method.[11] The active space always consists of 11 orbitals and 10 electrons corresponding to $4d5s5p$ orbitals on Ag and $1s$ orbital on H, with the addition of one orbital of the σ symmetry that is mostly of $6s$(Ag) character. We try two schemes of state-averaging: (1) orbitals are optimized specifically for the state of interest, (2) orbitals are equally averaged over seven singlet states (equal weight for each state component) arising from the $^2S(5s)$, ^2P, ^2D, and $^2S(6s)$ levels of Ag, namely the $1\,^1\Sigma^+$, $2\,^1\Sigma^+$, $3\,^1\Sigma^+$, $4\,^1\Sigma^+$, $1\,^1\Delta$, $1\,^1\Pi$, and $2\,^1\Pi$ states of AgH. In order to prevent variational collapse to the ground state in the case of the state-specific orbitals, we added 3% of the ground state density.

To take into account dynamical correlation, we use the recently developed spin–orbit multiconfigurational self-

TABLE I. Basis set for Ag: contracted functions $\chi_n=\Sigma_i c_{ni}x^{n_x}y^{n_y}z^{n_z}\times\exp(-\zeta_i r^2)$, where $n_x+n_y+n_z=l$, the orbital angular momentum.

Type	ζ_i	c_{1i}	c_{2i}	c_{3i}
s	32 467 592.6	0.000 542	−0.000 180	0.000 078
s	3 975 831.63	0.000 974	−0.000 324	0.000 140
s	1 154 270.38	0.001 246	−0.000 420	0.000 185
s	415 826.859	0.002 222	−0.000 740	0.000 314
s	163 308.086	0.003 914	−0.001 339	0.000 597
s	66 965.0084	0.007 323	−0.002 467	0.001 049
s	28 144.8955	0.015 592	−0.005 438	0.002 410
s	12 012.8492	0.033 185	−0.011 566	0.005 015
s	5180.307 34	0.074 581	−0.027 303	0.012 041
s	2250.034 66	0.157 571	−0.060 618	0.026 903
s	982.415 082	0.291 443	−0.129 541	0.058 476
s	430.630 645	0.368 624	−0.209 155	0.099 146
s	189.332 726	0.200 936	−0.140 217	0.069 328
s	83.440 4030	0.016 547	0.377 390	−0.247 406
p	66 817.8807	0.000 474	−0.000 215	0.000 085
p	11 041.0397	0.001 718	−0.000 783	0.000 308
p	3635.231 23	0.005 323	−0.002 439	0.000 969
p	1422.018 68	0.018 722	−0.008 659	0.003 408
p	595.962 652	0.061 270	−0.028 966	0.011 581
p	258.525 284	0.173 076	−0.085 091	0.033 871
p	114.377 718	0.360 471	−0.188 881	0.077 184
p	51.230 2340	0.406 531	−0.209 679	0.082 912
p	23.135 3250	0.154 161	0.150 337	−0.084 853
p	10.507 9960	0.008 640	0.605 149	−0.363 821
d	889.273 645	0.001 778	−0.000 566	
d	265.332 034	0.013 192	−0.004 246	
d	105.807 387	0.058 257	−0.018 807	
d	45.366 5020	0.188 273	−0.062 103	
d	20.024 0450	0.377 840	−0.121 915	
d	8.967 408 00	0.413 059	−0.116 052	

TABLE II. Basis set for Ag, exponents for uncontracted functions.

s	p	d	f	g
36.842 6670	4.792 684 00	4.049 312 00	3.373 850 88	3.252 140 21
16.292 7800	2.192 798 00	1.837 998 00	1.519 123 80	1.485 272 32
7.214 241 00	1.005 693 00	0.837 160 00	0.684 006 86	0.678 332 95
3.197 758 00	0.462 120 00	0.382 227 00	0.307 983 71	
1.418 689 00	0.212 668 00	0.174 823 00		
0.629 880 00	0.097 990 00	0.080 066 00		
0.279 840 00	0.045 197 00			
0.124 396 00				
0.055 324 00				
0.024 615 00				

consistent field second-order quasidegenerate perturbation theory[12] (SO-MCQDPT). The spin–orbit coupling (SOC) effects are thus carefully considered, including dynamical correlation effects on SOC. We use the two-electron operator arising from the Breit–Pauli Hamiltonian;[13] the one-electron operator is taken from the spin-dependent one-electron RESC Hamiltonian, that adds further relativistic transformation of the Breit–Pauli Hamiltonian. In the SO–MCQDPT calculations we include all the 0^+ states, corresponding at the dissociation limit to the $^2S(5s)$, ^2P, ^2D, and $^2S(6s)$ terms of Ag; namely, the $1\,^1\Sigma^+$, $2\,^1\Sigma^+$, $3\,^1\Sigma^+$, $4\,^1\Sigma^+$, $1\,^3\Pi$, and $2\,^3\Pi$ states of AgH. $^1\Delta$ is also included although it has $\Omega=2$ and does not couple to the 0^+ states. We include it to avoid otherwise necessary geometry-dependent hand manipulations excluding this state from other states of the same symmetry in C_{2v}. Since it does not couple to any 0^+ state it has no direct influence upon the results. (There is, however, some small influence through the orbital canonicalization procedure in MCQDPT.) The orbitals used in SO–MCQDPT calculations are taken from CAS; we canonicalize them using the generalized Fock operator with the one-particle density averaged over all the states included in SO–MCQDPT.

Now we describe in detail the difference between several ways to do CASSCF and SO–MCQDPT that we have tried.

1. SO–MCQDPT with orbitals from state-specific CASSCF (CAS-a)

In CASSCF, we have averaged 3% of $X\,^1\Sigma^+$ and 97% of $A\,^1\Sigma^+$. In the CASSCF optimization we have 11 orbitals: six a_1, one a_2, two b_1 and two b_2, in C_{2v}. The converged orbitals correspond to $4d5s5p6s$ of Ag and $1s$ of H except for one orbital switch, namely the core $4p_z$ orbital replacing the active $4d_{x^2-y^2}$ orbital. The occupation number of $4p_z$ is very close to 2 at all distances; similarly, we have found in calculations where $4d_{x^2-y^2}$ is present in the active space (CAS-*b*) that its occupation number is also very close to 2. The discrepancies between the CAS-*a* and CAS-*b* potential energy curves that are given in Sec. III A come from two sources. First, the $4d_{x^2-y^2}\rightarrow 4p_z$ orbital switch provides an extra freedom in taking into account nondynamical correlation: the chemically active $4p_z$ orbital is more important for description of the σ bond in $A\,^1\Sigma^+$ of AgH than the chemically passive $4d_{x^2-y^2}$ orbital; the difference, however, is rather small. The second difference is somewhat larger and it comes from different ways of treating dynamical correlation in the MCQDPT calculations where the CAS-*a* and CAS-*b* wave functions are used as a reference function. As can be seen below, the inclusion of the $4p_z$ orbital into the active space turns out to be a significant improvement in describing the $A\,^1\Sigma^+$ state, as the shelf-like part of the potential is very sensitive to the correlation of a_1 orbitals. In the $A\,^1\Sigma^+$ state of AgH, the $5p_z$ orbital is populated but the $5p_x$ and $5p_y$ orbitals on Ag are unoccupied; because of that the two unoccupied $5p_x$ and $5p_y$ orbitals are heavily mixed with $5d$ and $4f$ orbitals on Ag of the same molecular symmetry. Thus, this approach, while getting state-specific orbitals for the state of primary interest ($A\,^1\Sigma^+$), does not treat high-lying excited states equally well.

2. SO-MCQDPT with orbitals from state-specific CASSCF (CAS-b)

Like in the CAS-*a* case, we average 3% of $X\,^1\Sigma^+$ and 97% of $A\,^1\Sigma^+$. By using a different set of starting orbitals, we have been able to converge CASSCF to the 11 orbitals corresponding to $4d5s5p6s$ of Ag and $1s$ of H. The $4s$ and $4p$ core orbitals of Ag are correlated using MCQDPT. Similarly to the CAS-*a* case, two virtual $5p_x$ and $5p_y$ orbitals are heavily mixed with the $5d$ and $4f$ orbitals on Ag of the same molecular symmetry.

3. SO-MCQDPT with the state-averaged CASSCF orbitals

Due to state averaging, which effectively populates all active orbitals, the converged CASSCF orbitals correspond perfectly to $4d5s5p6s$ on Ag and $1s$ on H. Since preliminary calculations showed a very small effect of core correlation we do not correlate the $4s$ and $4p$ orbitals on Ag in the MCQDPT calculation.

As perturbation theories are known to suffer from intruder states, we use the recently developed intruder state avoidance (ISA) technique.[14] The two shift parameters used in ISA are set to 0.02 for the spin-free terms, and 0.1 for the spin–orbit terms. As found by Witek *et al.*,[14] these values have only a very small effect upon the second-order multireference Møller-Plesset perturbation theory (MRMP)[15–18] energies, except where intruder states are present; ISA produces smooth potential energy curves eliminating problems related to the quasidegeneracies occurring in the spectrum of the zeroth-order Hamiltonian. In our calculations, we find an intruder state located very close to the equilibrium distance that came in through the off-diagonal elements of the effective MCQDPT Hamiltonian. This type of intruder states is more complex compared to the MRMP intruder states.

For all the calculations of potential energy surfaces, the GAMESS[19] suite of programs is used. An analytical function including the Morse potential and linear combinations of Gaussians, is fitted to the calculated energies. This analytical fit is then used to compute numerically the vibrational energy levels (see below). Rotational constants B_v are computed by numerical integration of $B=1/2\mu R^2$ with the vibrational eigenfunctions $\psi_v(R)$. Here, $\mu=0.998\,412\,89$ is the reduced mass and R the internuclear separation.

B. Computation of vibrational levels

We solve the nuclear Schrödinger equation in the adiabatic approximation for the $A\,^1\Sigma^+$ state, which is represented by the analytical fit. The determination of the vibrational energy levels is made by direct diagonalization of the Hamiltonian matrix. The basis set used consists of sine functions $|S_n\rangle$, $n=1,\ldots,N$

$$\langle R|S_n\rangle=\sqrt{\frac{2}{R_>-R_<}}\sin\frac{n\pi(R-R_<)}{(R_>-R_<)}, \tag{2.2}$$

for which the kinetic energy operator is diagonal

$$-\frac{d^2}{dR^2}|S_n\rangle=\frac{n^2\pi^2}{(R_>-R_<)^2}|S_n\rangle. \tag{2.3}$$

This spectral representation is associated to the discrete variable representation[20,21] (DVR), $|R_p\rangle$, $p=1,...,P$, by means of the collocation matrix

$$U_{pn}=\sqrt{\frac{2}{P+1}}\sin\frac{n\pi(R_p-R_<)}{(R_>-R_<)}. \tag{2.4}$$

In this DVR, based on the regular grid $\{R_p=R_<+p(R_>-R_<)/(P+1),p=1,...,P\}$, the matrix representation of the potential operator is diagonal. Therefore, one can easily express the matrix elements for the potential in the initial sine basis set

$$\langle S_n|V(R)|S_{n'}\rangle=\sum_{p=1}^{P}U_{pn}V(R_p)U_{n'p}. \tag{2.5}$$

The Hamiltonian matrix in the $|S_n\rangle$ basis set is obtained by adding the kinetic [Eq. (2.3)] and the potential [Eq. (2.5)] terms; its diagonalization yields vibrational levels (eigenvalues) and nuclear wave functions (eigenvectors).

The accuracy of the collocation scheme is controlled by using a larger number of grid points P than the number of the initial sine functions N. The choice of the range $[R_<,R_>]$ is made such as the eigenfunctions of interest are null outside the working box. The values of the parameters used for the computation of vibrational levels of the $A\,^1\Sigma^+$ state of AgH are $N=191$, $P=195$, and $[R_<,R_>]=[1.058\ 354\ \text{Å},9.525\ 186\ \text{Å}]$.

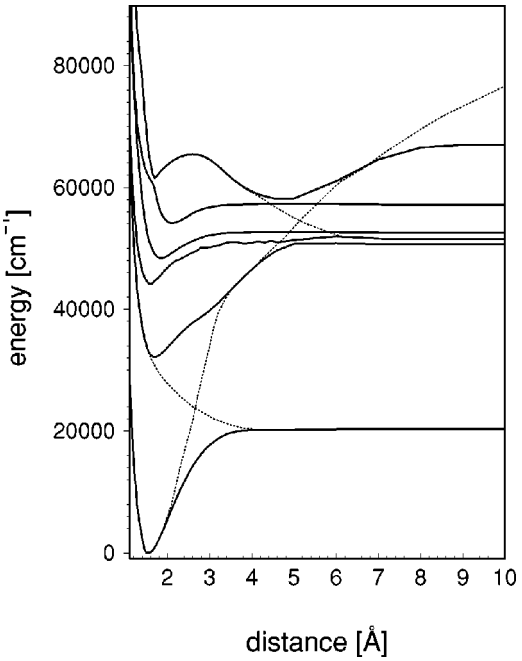

FIG. 1. Six lowest 0^+ states obtained from the SO–MCQDPT calculation using the state-averaged orbitals. Avoided crossings responsible for the unusual shape of the $A\,^1\Sigma^+$ potential are plotted schematically using dotted lines. The dissociation limit corresponding to Ag^+H^- (the highest dotted line) is out of the range of this plot.

III. RESULTS

A. Potential energy surfaces

Potential energy curves of the lowest six 0^+ states of AgH calculated using the SO–MCQDPT method with a set of state-averaged CASSCF orbitals are shown in Fig. 1. The two lowest and two highest curves correspond to the $^1\Sigma^+$ states; the other two are the 0^+ components of the two $^3\Pi$ states. As readily seen from Fig. 1, the $A\,^1\Sigma^+$ curve—corresponding to the second 0^+ curve in the SO–MCQDPT calculations—has a rather peculiar shape. As we show below, this shape is due to avoided crossings. The dominant electronic configuration for this state is $[\text{core}]4d^{10}\sigma^1\sigma^{*1}$ at short distances and $[\text{core}]4d^{10}5p^1 1s^1_{\text{H}}$ at long distances. For intermediate distances—where the observed peculiarity in the $A\,^1\Sigma^+$ curve occurs—a large contribution of the ionic-like $[\text{core}]4d^{10}1s^2_{\text{H}}$ configuration is found. This configuration corresponds at smaller distances to the dominant configuration of the $X\,^1\Sigma^+$ ground state, namely to $[\text{core}]4d^{10}\sigma^2$. Therefore, at the region of 2.5–3.5 Å, an avoided crossing of the $X\,^1\Sigma^+$ and $A\,^1\Sigma^+$ states occurs; schematical curves corresponding to noninteracting configurations are plotted in Fig. 1 using a dotted line. Another avoided crossing occurs at the distance around 5 Å: the analysis of the $A\,^1\Sigma^+$ and $C\,^1\Sigma^+$ wave functions shows that their main configurations interchange; a schematical plot corresponding to this avoided crossing is also given in Fig. 1 with a dotted line. A detailed analysis of the $A\,^1\Sigma^+$ state wave function is performed in Sec. III C, for the calculations employing a set of the CAS-*a* state-specific CASSCF orbitals. Spectroscopic parameters for the states from Fig. 1—obtained by fitting the equilibrium and dissociation parts of the curves to the Morse potential—are listed in Table III along with experimental and the previous[6] theoretical results. We note that the small bumps occurring in the third 0^+ state in Fig. 1 correspond to the removed intruder states that heavily plague that particular excited state.

The SO–MCQDPT calculations with a set of state-specific orbitals yield a noticeably more accurate potential for the $A\,^1\Sigma^+$ state, compared to the state-averaged CASSCF orbitals. We have performed many different sets of preliminary calculations employing different active spaces and canonicalization schemes; we have also used different ways of correlating the core orbitals. The best potential—in terms of its vibrational levels—is obtained in calculations denoted by CAS-*a* (see Sec. II A1). Spectroscopic parameters obtained for this potential are listed in Table IV together with the results for the state-specific CAS-*b* and state-averaged potentials. The correspondence of the CAS-*a* potential spectroscopic parameters to the experiment is good except for ω_e, which is overestimated by 200 cm^{-1}. Very good value of ω_e is found for the CAS-*b* potential: the difference to the experiment is only 60 cm^{-1}. The CAS-*b* potential reproduces the equilibrium region very well, while rather large discrepancies are observed for longer internuclear separations. The potential energy curve for the $A\,^1\Sigma^+$ state of AgH calculated with the state-specific CAS-*a* orbitals is shown in Fig. 2 at various levels of theory. Dynamic correlation is shown to play a very important role for $A\,^1\Sigma^+$: the dissociation limit is shifted up by more than 6500 cm^{-1} and the potential is much steeper. Coupling of the $^1\Sigma^+$ states after including dynamical correlation is found to have a rather small influence on the potential: the MRMP and MCQDPT curves dif-

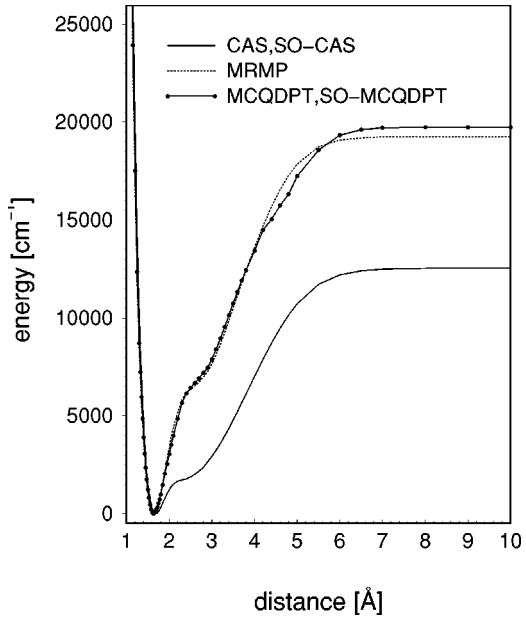

FIG. 2. Potential energy curve for the $A\ ^1\Sigma^+$ state of AgH at different levels of theory. The dynamical correlation effects are very significant, while the spin–orbit effects are negligible.

fer only in the dissociation region. As can be seen from Fig. 2—where the curves for the CAS and SO–CAS calculations and for the MCQDPT and SO–MCQDPT calculations coincide–the spin–orbit effects do not modify the $A\ ^1\Sigma^+$ potential, either on the nondynamical or dynamical correlation level; the effect of spin–orbit coupling is of the order of 10 cm^{-1} except for the dissociation limit, where it increases to several hundreds, having a very weak influence upon the low vibrational levels but some influence upon the dissociation energy.

B. Vibrational levels and rotational constants

Vibrational levels and rotational constants of $A\ ^1\Sigma^+$ are calculated for the following SO–MCQDPT potentials: state averaged SA, state-specific CAS-*a*, and state-specific CAS-*b*. For completeness of our study, we have also included in our investigations the semiempirical potential constructed graphically by Learner.[3] Since no numerical data are available for this potential, the curve presented in Fig. 3 of Ref. 3 has been digitized manually. Such a procedure introduces some error, thus the vibrational levels and rotational constants calculated for this potential have only an approximate character. The analytical form of the fitted potentials is given in Table V as a sum of a Morse potential and a number of Gaussian-like terms. The calculated vibrational levels for all investigated potentials are listed in Table VI; the calculated rotational constants are given in Table VII. The potential energy curves are plotted in Fig. 3. For each curve, the lowest ten vibrational levels are displayed; the levels for which the experimental data exist are plotted using solid lines. A direct comparison of calculated and experimental vibrational levels is rather tedious; a much clearer picture is often obtained from the Birge–Sponer diagram. This plot, giving a relationship between the vibrational interval $\Delta G(v+\frac{1}{2})$ and the vibrational quantum number v, is shown in Fig. 4. As readily visible, the approximately linear relationship expected for the usual Morse-like potential is preserved only for the lowest vibrational levels. For higher levels, a change in the slope of the curve is observed for both the experimental and the calculated potentials. A similar feature is observed for the rotational constants B_v in Fig. 5: the usual linear character of the relationship between B_v and v is preserved only for the lowest few vibrational levels.

None of the presented potentials reproduces the experimental results exactly; the best correspondence is found for the CAS-*a* state-specific SO–MCQDPT potential presented in Fig. 3(b). Despite its too large steepness in the equilibrium region—the CAS-*a* vibrational levels are located a few hundred wave numbers over the experimental levels—all the characteristic features observed in the experiment are reproduced well. The v dependence of vibrational intervals in Fig. 4 and rotational constants in Fig. 5 is similar to the experimental dependence. Moreover, the largest change in the slope of the CAS-*a* curves presented in Figs. 4 and 5 is observed for $v=5$, similarly, to the experiment. Therefore, we conclude that among all the investigated potentials, the SO–MCQDPT curve obtained using a set of the CAS-*a* state-specific orbitals [Fig. 3(b)] is the best approximation to the real potential energy surface.

We should devote, (for the end of this section) some attention to vibrational levels and rotational constants obtained for the potential shown in Fig. 3(a). This curve was derived graphically by Learner[3] on the basis of the observed

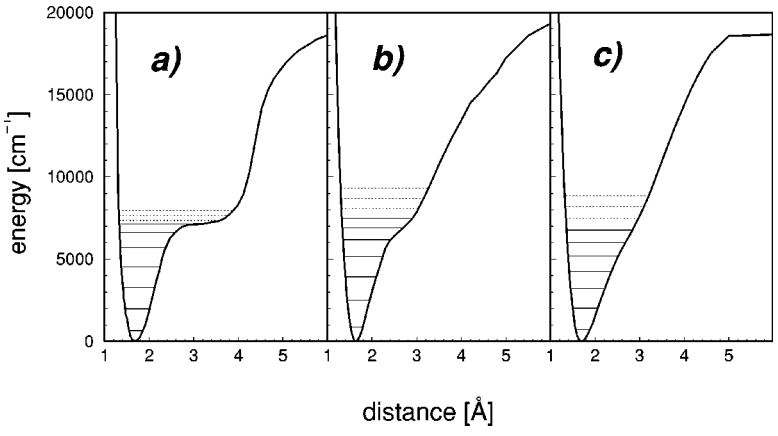

FIG. 3. Potential energy curve for the $A\ ^1\Sigma^+$ state of AgH: (a) constructed graphically by Learner (Ref. 3), (b) calculated using SO–MCQDPT with the CAS-*a* state-specific orbitals, and (c) calculated using SO–MCQDPT with the state-averaged orbitals. Vibrational levels for each curve are obtained by numerical integration. Levels printed with dotted line were not observed in experiment.

TABLE III. Spectroscopic constants for the 0^+ states of AgH (theoretical values assuming the Morse potential shape near the equilibrium). "Label" represents major *LS* coupling state in the given 0^+ state. T_e are the excitation energies (from the minimum of the ground state to the minimum of the excited state), r_e are equilibrium distances, B_e are rotational constants, D_e are dissociation energies, and ω_e and $\omega_e x_e$ are vibrational constants. All quoted experimental D_e values were obtained from D_0 values using $D_e = D_0 + \omega_e/2$. In the case of two subscripts over D_e values, the first indicates the reference for D_0 and the second for ω_e. Calculated values of B_e were computed using $B_e = 1/2\mu r_e^2$. Value with 0 subscript indicate constants with $v = 0$ rather than at the equilibrium (e.g., B_0 instead of B_e). Uncertain experimental values are marked with $>$, $<$ and ? signs.

Label		T_e (cm^{-1})	r_e (Å)	B_e (cm^{-1})	D_e (cm^{-1})	ω_e (cm^{-1})	$\omega_e x_e$ (cm^{-1})
	calc.[a]	0	1.564	6.904	20 387.0	2073.0	52.7
$X\ ^1\Sigma^+$	calc.[b]		1.620	6.43		1902.0	
	exp.	0	1.618[c]	6.449[c]	21 200[d,c]	1759.9[c]	34.06[c]
	calc.[a]	32 208.0	1.717	5.730	18 544.0	1422.0	27.3
$A\ ^1\Sigma^+$	calc.[b]		1.604	6.56		1805.0	
	exp.	29 959.0[c]	1.638,[e] 1.665[c]	6.265[e]	19 100[f,e]	1663.6[e]	87.0[e]
	calc.[a]	44 305.0	1.594	6.644	7341.0	1620.0	89.4
$a\ ^3\Pi$	calc.[b]		1.594	6.64		1742.0	
	exp.	41 700.0[c]	$<$1.64[d]	$>$6.3?[d]	$>$9700[d,c]	1450?[c]	50?[c]
	calc.[a]	48 490.0	1.845	4.960	4153.0	1198.0	86.4
$c_1\ ^3\Pi$	calc.[b]		1.813	5.13		1320.0	
	exp.	47 472.0[d]	1.85[d]	$>4.95_0$[d]	7500		
	calc.[a]	54 236.0	2.093	3.856	3033.0	1026.0	86.8
$B\ ^1\Sigma^+$	calc.[b]		2.050	4.01		1271.0	
	exp.	44 510.0[d]	1.862[d]	4.87[d]	6600.0[d]	1220.0[d]	65.0[d]
$C\ ^1\Sigma^+$	calc.[a]	58 218.0	4.596	0.7995	10 026.0	433.0	4.7

[a]SO–MCQDPT with state averaged orbitals (this work).
[b]MRMP with state specific orbitals, by Witek *et al.* (Ref. 6).
[c]Huber and Herzberg (Ref. 22).
[d]Ringström and Åslund (Ref. 4).
[e]Bengtsson and Olsson (Ref. 1).
[f]Learner (Ref. 3), $D_0 = 18\,250.0 \pm 500\ cm^{-1}$.

vibrational levels; two unobserved levels—with $v = 10$ and $v = 16$—that were inferred from the modified Birge–Sponer diagram were used as well. (For more details, see Ref. 3) Learner did not calculate any vibrational levels for the potential he proposed; an attempt to obtain them was made, but numerical difficulties and "lack of time prevented an adequate investigation of this problem." [3] Vibrational levels and rotational constants corresponding to the potential suggested by Learner are calculated in the present study; their correspondence to the experiment is rather crude. This is most visible from Figs. 4 and 5: the curves corresponding to Learner's potential differ distinctly from the other presented curves. The difference is largest for $v = 6$ where a sharp, unphysical change of the vibrational interval curve is observed. These large discrepancies can have a source only in the wrong form of the potential, both in the equilibrium and the shelf-like regions; errors related to a process of manual scanning are only on the order of a few cm^{-1} and they are too small to bring about such big discrepancies in the calculated vibrational levels and rotational constants.

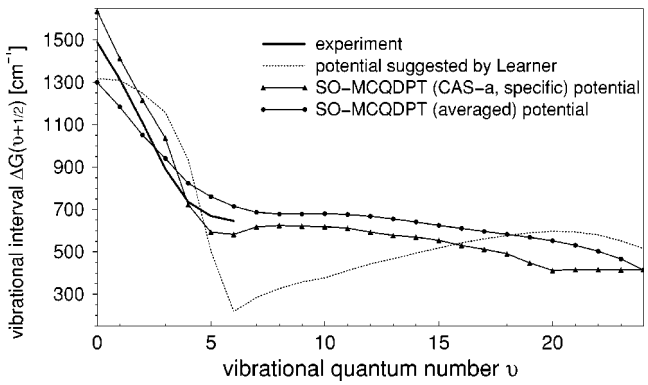

FIG. 4. The Birge–Sponer diagram for the $A\ ^1\Sigma^+$ state of AgH. The calculated values are obtained from numerical integration of potential energy curves.

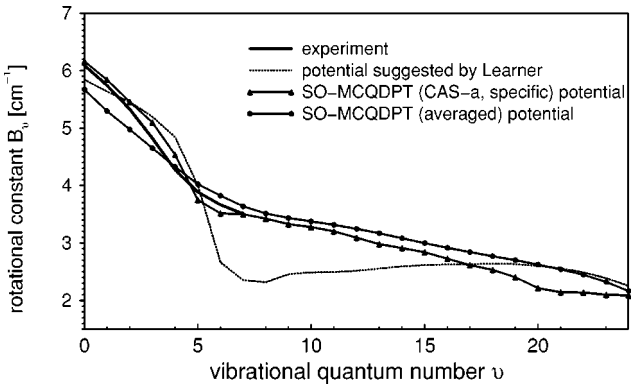

FIG. 5. Plot of rotational constant B_v as a function of vibrational quantum number v. The calculated values are obtained from numerical integration of potential energy curves.

TABLE IV. Spectroscopic constants for the $A\,^1\Sigma^+$ state (theoretical values from numerical integration of the energy curve).

	r_e (Å)	B_e (cm^{-1})	α_e (cm^{-1})	D_e (cm^{-1})	ω_e (cm^{-1})	$\omega_e x_e$ (cm^{-1})
This work[a]	1.6398	6.3204[e]	0.3197[e]	19 722.2	1860.6[f]	111.7[f]
This work[b]	1.6263	6.4230[e]	0.3838[e]	17 527.2	1604.2[f]	54.7[f]
This work[c]	1.6990	5.8542[e]	0.3718[e]	18 510.8	1415.5[f]	57.8[f]
MRCI[d]	1.607	⋯	⋯	⋯	1590.0[g]	
Exp.[h]	1.638	6.265	0.348	19 100	1663.6[f]	87.0[f]

[a]SO–MCQDPT with orbitals from state specific CASSCF (CAS-*a*).
[b]SO–MCQDPT with orbitals from state specific CASSCF (CAS-*b*).
[c]SO–MCQDPT with orbitals from state averaged CASSCF.
[d]Configuration selected MRCI with SCF $X\,^1\Sigma^+$ orbitals by Hess and Chandra (Ref. 5).
[e]B_e and α_e values estimated from rotational constants B_0 and B_1 using the relation $B_v = B_e - \alpha_e(v+1/2)$.
[f]Fitting Morse levels $E_1 - E_0$ and $E_2 - E_0$, where $E_v = \omega_e(v+1/2) - \omega_e x_e(v+1/2)^2$, to vibrational levels $\tilde{E}_1 - \tilde{E}_0$ and $\tilde{E}_2 - \tilde{E}_0$ ($\tilde{E}_0$ per se is not known experimentally); $\tilde{E}_v$ are levels from the numerical integration of the energy curve(calculation) or measured levels (experiment).
[g]Using polynomial fit for several points near the equilibrium.
[h]All values are due to Bengtsson and Olsson (Ref. 1) except for D_e that he did not provide. The quoted value is from Table III, q.v. for details.

TABLE V. Parameters for the fitted potentials. The form of the potential is $V(R) = D_e(1 - e^{-a(R-R_e)})^2 + \Sigma_k c_k e^{-d_k(R-s_k)^{n_k}}$.

	Parameters for the Morse-like part of the potential		
Potential	D_e (cm^{-1})	a ($Å^{-1}$)	R_e (Å)
SA	18 510.4	1.378 00	1.699 00
CAS-*b*	17 516.6	1.507 03	1.626 27
Learner's graphical	18 915.1	1.269 04	1.688 83
CAS-*a*	19 727.1	1.570 29	1.639 77

Parameters for the Gaussian-like part of the potential

SA potential

c_k (cm^{-1})	d_k ($Å^{-1}$)	s_k (Å)	n_k
−4149.9	1.604 05	3.454 89	2
−2694.0	3.130 02	2.749 98	2
437.2	1.000 92	5.277 84	2
627.6	8.432 66	2.848 88	2
32 353.6	2.595 50	3.510 33	2
−32 334.5	2.515 19	3.525 26	2
−100.5	60.4372	2.227 92	2
234.8	131.841	1.439 31	2
182.3	47.6587	1.804 57	2

CAS-*b* potential

c_k (cm^{-1})	d_k ($Å^{-1}$)	s_k (Å)	n_k
−4833.1	1.101 57	3.112 64	2
11 950.8	17.750 3	0.927 597	2
1250.7	0.286 771	3.855 43	2
131.7	168.079	1.340 18	2
299.3	37.6849	1.789 88	2
586.8	12.3561	2.321 04	2
−264.0	7.835 03	3.906 87	2
278.2	31.9279	4.478 09	2

CAS-*a* potential

c_k (cm^{-1})	d_k ($Å^{-1}$)	s_k (Å)	n_k
−140.1	208.304	2.163 20	2
−164.6	80.0000	1.200 00	2
347.3	68.1244	1.802 03	2
−374.8	88.0964	1.797 96	2
384.1	20.0000	4.290 00	2
−139.1	100.000	4.804 11	2
−5646.9	2.288 58	2.963 75	2
−4873.2	0.829 09	4.028 82	2
−2887.6	24.7319	1.091 74	2
−266.4	22.3853	2.494 40	2
−257.7	26.1765	3.675 26	2
−275.7	2.724 97	5.636 12	2
336.6	26.7988	1.832 27	2
142.8	180.134	1.480 24	2
229.0	24.5530	3.097 81	2

Learner's graphical potential

c_k (cm^{-1})	d_k ($Å^{-1}$)	s_k (Å)	n_k
2015.8	7.688 55	4.6493	2
−1286.1	3.559 78	2.901 30	2
781.5	5.834 11	2.418 26	2
134.4	15 517.2	2.374 33	4
−8720.4	0.976 31	3.866 08	2
123.8	4372.24	1.747 47	4
35.9	20.493 72	1.990 00	2
−32.9	60.0000	3.240 00	2
43.9	62.2400	2.930 00	2
−97.4	90.493 72	2.600 00	2
83.4	50.2800	3.802 88	2
−51 069.5	16.7501	4.441 00	2
51 283.2	17.0043	4.441 48	2
36 310.0	5.670 12	5.023 19	2
−36 576.9	5.486 79	5.014 74	2
1157.13	8.887 97	4.666 61	2
−127.9	3 000 000.0	1.455 00	4
105.6	4771.10	1.513 93	2
64.4	842.907	2.230 52	2
175 741.0	68.8595	1.038 82	2

TABLE VI. Vibrational levels E_v of the $A\,^1\Sigma^+$ state relative to E_0 (in cm^{-1}). Different number of levels given for SO–MCQDPT correspond to different D_e value for each column. Standard deviation is computed with respect to experimental data.

v	Graphical[a]	SO–MCQDPT[b]	SO–MCQDPT[c]	SO–MCQDPT[d]	Exp[1]
1	1317.2	1636.7	1489.4	1300.0	1489.6
2	2628.1	3050.1	2864.0	2484.5	2805.2
3	3877.6	4266.3	4190.0	3536.3	3914.6
4	5035.0	5303.4	5409.9	4477.4	4806.8
5	5971.4	6027.0	6459.5	5301.3	5542.3
6	6473.6	6620.2	7308.6	6062.3	6211.4
7	6691.2	7202.4	8051.3	6777.5	6857.2
8	6976.1	7819.9	8758.8	7664.7	
9	7302.6	8444.3	9442.5	8142.7	
10	7659.8	9064.9	10 111.9	8821.9	
11	8037.6	9683.9	10 771.8	9501.8	
12	8449.4	10 295.9	11 422.7	10 178.0	
13	8892.5	10 889.4	12 063.3	10 845.9	
14	9360.6	11 466.8	12 691.2	11 501.5	
15	9854.0	12 036.0	13 305.0	12 142.3	
16	10 372.1	12 590.3	13 904.6	12 767.3	
17	10 915.0	13 120.6	14 490.8	13 377.5	
18	11 477.0	13 632.5	15 063.3	13 973.8	
19	12 053.9	14 123.5	15 620.0	14 556.5	
20	12 643.7	14 571.4	16 158.2	15 124.9	
21	13 240.2	14 983.7	16 673.2	15 676.4	
22	13 834.5	15 399.6		16 207.0	
23	14 415.1	15 816.0		16 710.3	
24	14 967.5	16 230.7		17 176.4	
25	15 483.1	16 647.1			
26	15 963.2	17 043.6			
27	16 407.7	17 407.9			
28	16 820.2	17 754.8			
29	17 194.5	18 067.9			
30	17 523.5	18 353.9			
31	17 825.3	18 603.3			
32	18 066.8	18 799.0			
33	18 176.6				
Standard deviation	237.5	372.8	747.7	261.1	

[a]Derived from the first few experimental vibrational levels by Learner (Ref. 3), $E_0=665.1\ cm^{-1}$.
[b]SO–MCQDPT with orbitals from state specific CASSCF (CAS-a), $E_0=879.6\ cm^{-1}$.
[c]SO–MCQDPT with orbitals from state specific CASSCF (CAS-b), $E_0=814.9\ cm^{-1}$.
[d]SO–MCQDPT with orbitals from state averaged CASSCF, $E_0=716.6\ cm^{-1}$.

C. Explanation of the $A\,^1\Sigma^+$ potential energy curve shape

In this section, we perform a CI analysis and a population analysis in order to explain the unusual shape of the $A\,^1\Sigma^+$ potential energy curve. The weights of dominant configurations in the $A\,^1\Sigma^+$ wave functions are plotted in Fig. 6 as a function of the interatomic separation. There are three dominant configurations for $A\,^1\Sigma^+$; their active space occupations are displayed in Fig. 6. The order of 11 active orbitals in the C_{2v} point group is as follows: six a_1, one a_2, two b_1, and two b_2. The chemically important orbitals—the third, fourth, and fifth orbitals, all of the a_1 symmetry—have different characters at different distances. The third orbital is a σ bonding orbital composed mainly of the silver $5s$ and hydrogen $1s$ atomic orbitals; there is also a small admixture of the silver $4d_{z^2}$ orbital. At larger distances, the chemical character of this molecular orbital is rather complex: at 2–3 Å it is predominantly the $1s$ orbital of hydrogen; at around 4 Å, it becomes a mixture of the silver $5s$ and hydrogen $1s$ orbitals with a large contribution from a diffused s orbital of Ag (probably $6s$); for large distances, the $5s$ orbital of Ag becomes dominant, giving in the dissociation limit a pure $5s$ atomic orbital of silver. The fourth orbital of the a_1 symmetry is the σ^* antibonding orbital; in the equilibrium region, it is mainly a mixture of the silver $5s$ and hydrogen $1s$ orbitals with some contribution from $5p_z$ of Ag. At larger distances, it is predominantly a mixture of the silver $5s$ and $5p_z$ orbitals. At around 3 Å, a large contribution from the hydrogen $1s$ orbital changes its chemical character. Finally, at around 4 Å, it becomes an almost pure $1s$ orbital of hydrogen. The fifth orbital of the a_1 symmetry can be described as follows: at short and intermediate distances, it is an antibonding mixture of $1s$ of H and $5p_z$ of Ag with some admixture of a diffused s orbital of Ag. From around 6 Å, this orbital becomes a pure $5p_z$ orbital of silver. A knowledge of the chemical character of these three orbitals allows us to analyze the wave function of the $A\,^1\Sigma^+$ state of AgH. The character of the $A\,^1\Sigma^+$ wave function agrees with the chemical

TABLE VII. Rotational constants B_v for the $A\,^1\Sigma^+$ state (in cm^{-1}). Standard deviation is computed with respect to experimental data.

v	Graphical[a]	SO–MCQDPT[b]	SO–MCQDPT[c]	SO–MCQDPT[d]	Exp.[1]
0	5.8387	6.1606	6.2311	5.6684	6.0905
1	5.6336	5.8409	5.8473	5.2966	5.7420
2	5.4540	5.4588	5.5951	4.9782	5.3282
3	5.1948	5.0983	5.3338	4.6523	4.8200
4	4.8376	4.5324	4.9809	4.3238	4.2720
5	4.0056	3.7493	4.4927	4.0224	3.8852
6	2.6616	3.5120	4.0189	3.8188	3.6605
7	2.3509	3.5002	3.7786	3.6362	3.5050
8	2.3188	3.4231	3.6077	3.5107	
9	2.4531	3.3255	3.4737	3.4357	
10	2.4897	3.2737	3.3675	3.3754	
11	2.4938	3.2034	3.2754	3.3131	
12	2.5130	3.0896	3.1878	3.2433	
13	2.5543	2.9803	3.0996	3.1654	
14	2.5919	2.9102	3.0101	3.0821	
15	2.6140	2.8382	2.9220	2.9974	
16	2.6257	2.7255	2.8386	2.9159	
17	2.6273	2.6147	2.7596	2.8397	
18	2.6371	2.5325	2.6799	2.7679	
19	2.6289	2.4033	2.5945	2.6974	
20	2.5998	2.2119	2.5024	2.6235	
21	2.5566	2.1391		2.5410	
22	2.4876	2.1378		2.4435	
23	2.3845	2.0965		2.3220	
24	2.2542	2.0843		2.1621	
25	2.1195	2.0430			
26	1.9873	1.9123			
27	1.8555	1.8112			
28	1.7412	1.7166			
29	1.5830	1.5704			
30	1.4632	1.4583			
31	1.3495	1.2937			
32	1.0173	0.9356			
33	0.5144				
Standard deviation	0.6016	0.1649	0.4244	0.2718	

[a]Derived from the first few experimental vibrational levels by Learner (Ref. 3).
[b]SO–MCQDPT with orbitals from state specific CASSCF (CAS-*a*).
[c]SO–MCQDPT with orbitals from state specific CASSCF (CAS-*b*).
[d]SO–MCQDPT with orbitals from state averaged CASSCF.

intuition, as expected for the first excited state of AgH, but only at small and large internuclear separations: it corresponds to the $[\mathrm{core}]4d^{10}\sigma^1\sigma^{*1}$ configuration at short, and to the $[\mathrm{core}]4d^{10}5p^1 1s^1_{\mathrm{H}}$ configuration at large distances. Surprisingly, at intermediate distances $A\,^1\Sigma^+$ has mainly an ionic character corresponding to Ag^+H^- rather than to AgH; the leading configuration is $[\mathrm{core}]4d^{10}1s^2_{\mathrm{H}}$. This means that in the region 4–6 Å, a partial charge transfer occurs in the $A\,^1\Sigma^+$ state of AgH. As discussed in Sec. III A, the occurrence of the ionic-like $[\mathrm{core}]4d^{10}1s^2_{\mathrm{H}}$ configuration in the $A\,^1\Sigma^+$ wave function is related to two avoided crossings: with $X\,^1\Sigma^+$ at around 3 Å and with $C\,^1\Sigma^+$ at around 5 Å.

This ionic character of the $A\,^1\Sigma^+$ state of AgH in the region 4–6 Å is confirmed by a population analysis of the CASSCF wave function. The total atomic populations on Ag and H are shown in Fig. 7. Both curves—corresponding to the Mulliken and Löwdin atomic populations—give similar results for the intermediate region, showing a partial transfer of an electron from Ag to H. A maximum of the charge transfer is observed at 4 Å. Figures 7 and 8 present the plots for CAS-*a*; corresponding plots for CAS-*b* look very similar. We would like to stress that the $4d_{x^2-y^2} \rightarrow 4p_z$ orbital switch described in Sec. II A does not have any significant influence on the presented Mulliken population analysis. Note that the origin of this electron transfer is rather electrostatic than chemical: as can be seen from Fig. 7, the chemical bond in AgH—also corresponding to a partial transfer of an electron from Ag to H—loses its bonding character already around 2.5 Å.

More detailed information about the charge transfer in the $A\,^1\Sigma^+$ state of AgH can be obtained from the shell population analysis. The Mulliken populations on the *s*, *p*, and *d* orbitals of H and the *s*, *p*, *d*, and *f* orbitals of Ag are plotted in Fig. 8 as a function of internuclear separation. In the bonding region—between 1 and 2.5 Å—changes in all curves can be observed. However, in the region where the charge transfer occurs, 3–5.5 Å, the only affected shells are *p* on Ag and *s* on H. Therefore, we can conclude that the charge transfer corresponds to a partial excitation of an electron from the silver $5p_z$ atomic orbital to the hydrogen $1s$ atomic orbital. The peculiar shape of the $A\,^1\Sigma^+$ potential energy curve arises thus as a superposition of a normal Morse-like poten-

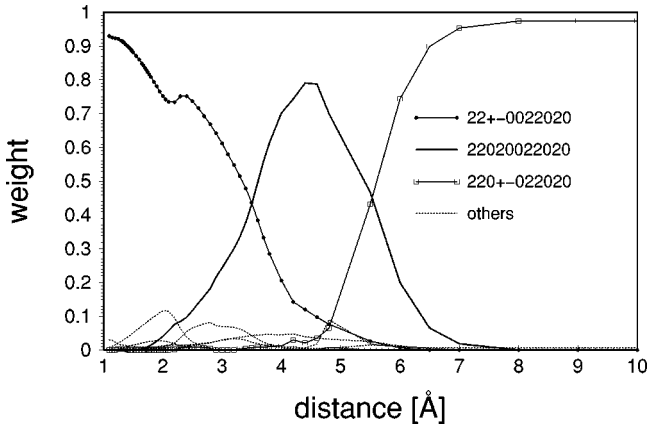

FIG. 6. Dominant configurations in the $A\,^1\Sigma^+$ state of AgH as a function of distance. Active orbitals are given in the following order: six of a_1, one of a_2, two of b_1 and two of b_2, in C_{2v} symmetry. For description of their chemical character, see text. The signs + and − denote an electron with the spin up or down, respectively.

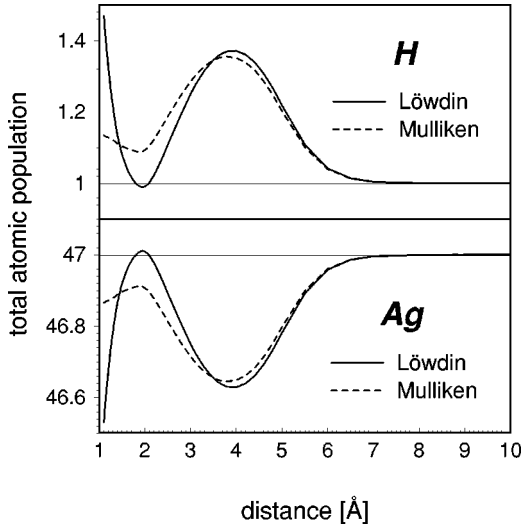

FIG. 7. Total Mulliken and Löwdin atomic populations for the $A\,^1\Sigma^+$ state of AgH as a function of internuclear separation. Note the ionic-like structure at around $R=4$ Å.

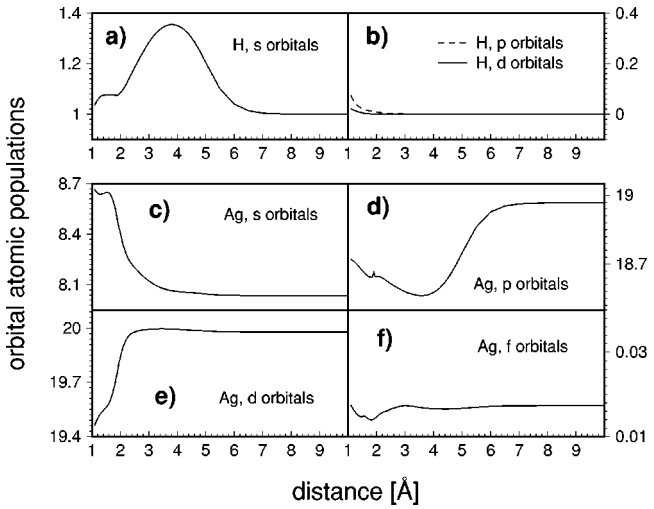

FIG. 8. Mulliken atomic populations for each shell of Ag and H in the $A\,^1\Sigma^+$ state of AgH. The ionic-like structure from Fig. 7 arises from a transition of electron from a *p* orbital of Ag to a *s* orbital of H.

tial corresponding to a covalent bond in AgH, and an electrostatic-driven interaction corresponding to a partial transfer of an electron from $5p_z$ of Ag to $1s$ of H occurring at the distance of 4–6 Å. The ionic-like $[\mathrm{core}]4d^{10}1s^2_{\mathrm{H}}$ configuration occurs in $A\,^1\Sigma^+$ due to two avoided crossings; they are plotted schematically in Fig. 1 using a dotted line.

IV. CONCLUSIONS

The potential energy curve of the $A\,^1\Sigma^+$ state of AgH is studied by means of the second-order SO–MCQDPT method. The best correspondence to the experiment is achieved when using a set of the state-specific CASSCF orbitals denoted by CAS-*a*; the curve obtained in this calculation is presented in Fig. 3(b). Vibrational intervals and rotational constants calculated for this curve agree well with the experiment. (For comparison, see Figs. 4 and 5.) An analysis of the $A\,^1\Sigma^+$ wave function shows a large contribution from the ionic-like $\mathrm{Ag}^+\mathrm{H}^-$ structure at internuclear distances between 4 and 6 Å; this structure corresponds to a partial transfer of an electron from the $5p_z$ orbital of silver to the $1s$ orbital of hydrogen. This ionic-like $[\mathrm{core}]4d^{10}1s^2_{\mathrm{H}}$ configuration occurs in $A\,^1\Sigma^+$ due to two avoided crossings; they are plotted schematically in Fig. 1 using dotted lines. The peculiar shape of the $A\,^1\Sigma^+$ potential energy curve is thus explained in terms of a superposition of two kinds of interactions: a Morse-like interaction corresponding to a covalent bond in AgH and an electrostatic interaction due to a partial charge transfer occurring at the interatomic separation of 4–6 Å.

Learner[3] suggested previously that the unusual shape of the $A\,^1\Sigma^+$ potential is due to an avoided crossing of $A\,^1\Sigma^+$ and $B\,^1\Sigma^+$. No evidence of such crossing is found in our calculations: the analysis of the $A\,^1\Sigma^+$ and $B\,^1\Sigma^+$ wave functions shows only a small mixing (approximately 10%) of their main configurations at the equilibrium region. We find, however, two other avoided crossings, namely $X\,^1\Sigma^+$ with $A\,^1\Sigma^+$ and $A\,^1\Sigma^+$ with $C\,^1\Sigma^+$, which have a fundamental influence on the $A\,^1\Sigma^+$ potential's shape. A critical analysis of the $A\,^1\Sigma^+$ potential energy curve constructed graphically by Learner does not confirm the validity of its shape: the calculated vibrational intervals and rotational constants show rather large discrepancies when compared to experimental data.

ACKNOWLEDGMENTS

D.G.F. wishes to thank JSPS for the fellowship award. H.W. would like to thank the Japanese Ministry of Education, Science and Culture for the scholarship.

[1] E. Bengtsson and E. Olsson, Z. Phys. **72**, 163 (1931).
[2] A. Gerö and K. Schmid, Z. Phys. **121**, 459 (1943).
[3] R. C. M. Learner, Proc. R. Soc. London, Ser. A **269**, 327 (1962).
[4] U. Ringström and N. Åslund, Ark. Fys. **32**, 19 (1966).
[5] B. A. Hess and P. Chandra, Phys. Scr. **36**, 412 (1987).
[6] H. A. Witek, T. Nakajima, and K. Hirao, J. Chem. Phys. **113**, 8015 (2000).
[7] M. Douglas and N. M. Kroll, Ann. Phys. (N.Y.) **82**, 89 (1974).
[8] R. J. Gdanitz and R. Ahlrichs, Chem. Phys. Lett. **143**, 413 (1988).
[9] T. Nakajima and K. Hirao, Chem. Phys. Lett. **302**, 383 (1999).
[10] T. H. Dunning, Jr., J. Chem. Phys. **90**, 1007 (1989).

[11] M. W. Schmidt and M. S. Gordon, Annu. Rev. Phys. Chem. **49**, 233 (1998).
[12] D. G. Fedorov and J. P. Finley, Phys. Rev. A **64**, 042502 (2001).
[13] H. A. Bethe and E. E. Salpeter, *Quantum Mechanics of One-and Two-Electron Atoms* (Plenum, New York, 1977).
[14] H. A. Witek, J. P. Finley, Y.-K. Choe, and K. Hirao, J. Comput. Chem. (in press).
[15] K. Hirao, Int. J. Quantum Chem. **S26**, 517 (1992).
[16] K. Hirao, Chem. Phys. Lett. **201**, 59 (1993).
[17] K. Hirao, Chem. Phys. Lett. **190**, 374 (1992).
[18] K. Hirao, Chem. Phys. Lett. **196**, 397 (1992).
[19] M. W. Schmidt *et al.*, J. Comput. Chem. **14**, 1347 (1993).
[20] J. C. Light, I. P. Hamilton, and J. V. Lill, J. Chem. Phys. **82**, 1400 (1985).
[21] C. Leforestier, J. Chem. Phys. **94**, 6388 (1991).
[22] K. P. Huber and G. Herzberg, *Constants of Diatomic Molecules* (Van Nostrand, New York, 1979).